Research Square

Preprints are preliminary reports that have not undergone peer review.
They should not be considered conclusive, used to inform clinical practice,
or referenced by the media as validated information.

In Vivo Ultrasound–MRI 3D Mapping of Neuromuscular Compartments Reveals the Neuromechanical Architecture of Finger-Specific Control

Dario Farina

d.farina@imperial.ac.uk

Imperial College London https://orcid.org/0000-0002-7883-2697

Yang Li

Shanghai Jiao Tong University

Yang Yu

Shanghai Jiao Tong University https://orcid.org/0000-0001-5582-4558

Yiming Kang

Shanghai Jiao Tong University https://orcid.org/0009-0002-9077-5207

Zongtian Yin

Shanghai Jiao Tong University

Shihan Ma

Imperial College London

Yuxuan Wei

Shanghai Jiao Tong University https://orcid.org/0009-0002-9466-3077

Qing Li

MR Research Collaborations, Siemens Healthineers Ltd.

Xinjun Sheng

Shanghai Jiao Tong University

Xiangyang Zhu

Shanghai Jiao Tong University https://orcid.org/0000-0003-4914-6636

Article

Keywords:

Posted Date: April 22nd, 2026

DOI: https://doi.org/10.21203/rs.3.rs-9301745/v1

License: This work is licensed under a Creative Commons Attribution 4.0 International License.
Read Full License

Additional Declarations: There is **NO** Competing Interest.

In Vivo Ultrasound–MRI 3D Mapping of Neuromuscular Compartments Reveals the Neuromechanical Architecture of Finger-Specific Control

Yang Li[1#], Yang Yu[1,2,3#], Yiming Kang[1], Zongtian Yin[1], Shihan Ma[4], Yuxuan Wei[1], Qing Li[5], Xinjun Sheng[1,2,3], Dario Farina[4*] and Xiangyang Zhu[1,2,3*]

[1]State Key Laboratory of Mechanical System and Vibration, School of Mechanical Engineering, Shanghai Jiao Tong University, Shanghai, China.
[2]Shanghai Key Laboratory of Intelligent Robotics, Shanghai Jiao Tong University, Shanghai, China.
[3]Meta Robotics Institute, Shanghai Jiao Tong University, Shanghai, China.
[4]Department of Bioengineering, Imperial College London, SW7 2AZ London, U.K.
[5]MR Research Collaborations, Siemens Healthineers Ltd., Shanghai, China.

[#]These authors contributed equally to this work.
[*]Corresponding author. Email: d.farina@imperial.ac.uk, mexyzhu@sjtu.edu.cn.

Abstract

Neuromuscular compartments provide the functional substrate for finger-specific motor control, yet their in vivo three-dimensional (3D) architecture remains unresolved because of the absence of clear fascial landmarks for imaging. As a representative example, in the flexor digitorum superficialis (FDS), the primary finger flexor, this lack of compartment-resolved anatomy and fiber trajectories limits our understanding of the neuromechanical control of hand movements and prevents realistic finger-specific computational models. Here, we present a multimodal imaging framework that combines ultrasound and magnetic resonance imaging (MRI) to resolve this gap by providing both volumetric compartment segmentation and in vivo architectural reconstruction. During isolated finger flexion, tissue movement directions estimated from dynamic ultrasound delineate compartment contours, which are mapped into a 3D MRI reference to generate volumetric compartment masks. Using these masks as constraints, tractography reconstructs 3D fiber trajectories and yields compartment-specific architectural measurements. When applied to ten healthy individuals, the framework yielded compartment topology and fiber orientations consistent with classic cadaveric anatomy. Moreover, the estimated compartments accurately predicted the experimental distribution of surface electromyography amplitude on the skin surface. These results demonstrate that in vivo compartment mapping can simultaneously resolve the missing in vivo anatomy and architecture of the FDS, providing 3D fiber trajectories and quantitative parameters for finger-specific computational models while delivering anatomically

grounded definitions of the functional units that underlie the neuromechanical control of the hand. By supplying compartment-level ground truth for both biomechanics and electromyography, this framework establishes a foundation for subject-specific neuromuscular digital twins and next-generation neuromuscular interfaces.

Introduction

Independent finger movement, a feature of human hand dexterity, relies on the selective recruitment of functional subunits within multi-tendon forearm muscles[1]. These subunits, referred to as neuromuscular, functional or muscle compartments[2, 3], are thought to provide the functional substrate for finger-specific motor control. Finger flexion is a key activity in daily life, mainly driven by the flexor digitorum superficialis (FDS), which contains four muscle compartments corresponding to the four digits[4, 5]. Because the FDS lies superficially in the forearm, it is especially relevant for surface electromyogram (EMG) recordings[6, 7] and clinical interventions[8, 9]. However, finger independence is jointly constrained by mechanical factors (e.g., intertendinous connections and myofascial coupling) and neural factors (e.g., common synaptic input to motoneurons)[10, 11, 12]. Elucidating these compartment-level constraints is fundamental to hand motor control, informing both basic research into neural control strategies[13] and translational applications such as human-machine interfaces for control and augmentation[14].

In contemporary views of motor control, muscles are no longer considered as the fundamental units of action. Instead, converging evidence from motor unit recordings and computational analyses[2, 3, 15] suggests that the central nervous system distributes common synaptic inputs to functional clusters of motor neurons that may span parts of one or several muscles, rather than whole muscles. These clusters act as low-dimensional control modules whose coordinated activity generates movement. Neuromuscular compartments provide a natural anatomical candidate for such modules. They are spatially distinct regions within a muscle that can receive partly independent neural drives and produce finger-specific mechanical actions[16]. Resolving the three-dimensional (3D) architecture of compartments in vivo is therefore not only an anatomical problem, but a prerequisite for neuromechanical investigations. It enables direct linking of motor neuron populations and their common inputs to the resulting compartment-level force production. By identifying and mapping compartments, one can move from a muscle-centric to a compartment-centric description of hand function, enabling neuromechanical questions to be posed at the level at which control is actually exerted[15]. This shift is crucial for addressing open questions in

neuromuscular control of the hand. For example, motor units recruited during isolated flexion of a single finger differ from those recruited when the same finger moves in combination with others[3], but this phenomenon has been difficult to interpret mechanistically because the spatial locations of the active motor units within the muscle are unknown. Compartment-resolved anatomy provides the missing context. It would indeed allow motor units to be assigned to specific compartments, so that changes in recruitment across single-finger and multi-finger tasks can be directly related to the underlying neuromechanical modules that generate hand movements.

To translate this compartment-centric view of motor control into quantitative frameworks, the anatomical modules targeted by motor neuron clusters must be explicitly represented in computational models of the neuromuscular system. Muscle compartment segmentation separates individual compartments from imaging data and thus provides the structural scaffold on which finger-specific physiological computational models can be built. In musculoskeletal modelling, hand models often estimate compartment architecture by scaling rather than direct measurement, which can lead to substantial errors in force output[17, 18]. Sensitivity analyses indicate that predicted muscle force is most sensitive to fiber length and physiological cross-sectional area[19], yet these compartment parameters remain inaccessible in vivo because neither compartment segmentation nor architectural measurement has been achieved. Modelling the electrical activity of muscle fibers (EMG modelling) further requires 3D muscle fiber trajectories within each compartment. Fiber trajectories determine the shape of action potentials, and the superposition of action potentials forms the EMG[13]. However, current simulations typically simplify fibers as curves of constant length, whereas real muscle exhibits variable fiber lengths and pennation angles[20]. Recent digital-twin work highlights the lack of realistic fiber trajectories as a key bottleneck limiting EMG simulation fidelity[13, 21].

Finally, our limitations in accurately modelling muscle compartments for finger control impact the design of human-machine interfaces based on EMG activity from the forearm. Because digit-related muscles are anatomically crowded[22, 23], their skin-surface electric field activation maps overlap substantially during finger movements[10], but this phenomenon has not been quantitatively linked to underlying anatomy. Consequently, it is not possible to assign EMG channels to finger-specific control and this problem is further exacerbated by the lack of anatomical references[13]. Similarly, compartment architectural information is also needed for precise targeting in functional electrical stimulation[8, 9] and for clinical assessment[24, 25]. Together, volumetric muscle compartment segmentation and the derived fiber trajectories and architectural parameters represent a shared

bottleneck across these applications.

Despite this need, in vivo volumetric compartment segmentation remains fundamentally challenging because muscle compartments are not separated by reliably visible anatomical boundaries. The compartment fascia can indeed be sub-millimeter thin or even absent. As a result, compartments are best defined functionally, requiring movement-based markers[26]. However, no single imaging modality can provide both dynamic functional markers and a full 3D anatomical reference. For example, magnetic resonance imaging (MRI) protocols, including movement-enhanced T2-weighted imaging and elastography[26, 27], have inferred compartment behavior but only on a single cross-section and without validation. Surface EMG can localize activation regions[10, 28] and ultrasound imaging can capture dynamic finger-specific muscle movement[29], yet both lack volumetric anatomical context, as well as the derived fiber trajectories and architectural parameters. Extending ultrasound to three dimensions does not overcome this fiber reconstruction barrier[30]. Consequently, current methods segment the compartments only in two dimensions and without validation. The absence of volumetric segmentation substantially limits our fundamental understanding of neuromuscular control in dexterous tasks and, therefore, the building of digital twins for both mechanical actions and biophysical signals. In turn, this limitation blocks downstream applications. The ability to detect compartments in 3D would open a new era of neuromechanical research, modelling, and interfacing.

To solve this challenge, we developed a multimodal imaging framework that exploits the complementary strengths of ultrasound and MRI to obtain in vivo compartment-resolved architecture of the FDS. Dynamic ultrasound during individual finger movements captures compartment-specific deformation, while MRI provides a 3D anatomical reference. Advanced image registration then links the two imaging domains. With image registration, the two-dimensional (2D) ultrasound annotations are indeed mapped into the MRI space to generate volumetric compartment masks. Within these masks, diffusion tensor imaging tractography completes the 3D reconstruction by determining muscle fiber trajectories and compartment-specific architectural parameters. This multimodal imaging measurement method was validated at both the segmentation and architectural levels. The complete study roadmap is summarized in **Supplementary Movie 1**.

Results

In vivo muscle compartment segmentation and fiber reconstruction

To reveal the correspondence between internal architecture of the FDS and its functional output, we constructed an in vivo multimodal analysis pipeline integrating ultrasound and MRI (**Fig. 1b**). The pipeline comprises three components: muscle compartment segmentation (here termed piecewise segmentation), architectural measurement, and validation.

Piecewise segmentation exploited the high temporal resolution of ultrasound to capture compartment-specific deformation elicited by isolated finger movements, thereby circumventing the inability of static MRI to resolve neuromuscular compartments. The segmentation pipeline comprised the steps of annotation, registration and lofting (**Fig. 2b, c**). First, we estimated a tissue movement direction field in the ultrasound sequence using optical flow and annotated compartment boundaries during isolated finger movements via a region growing strategy (**Supplementary Methods 1**). As shown in **Supplementary Movie 2**, this procedure accommodated dynamic deformation during contraction and reliably identified the functional boundaries of the index, middle, ring and little compartments. Next, a minimum-energy matching algorithm based on topological invariance registered the 2D ultrasound slices to the 3D MRI volume. Lofting interpolation across multiple transverse planes then produced continuous volumetric compartment masks. Seed point sampling experiments further demonstrated robustness to the choice of initial seeds (**Supplementary Fig. 5-8**).

After obtaining volumetric compartment masks, we performed tractography using diffusion tensor imaging under compartment constraints to reconstruct muscle fiber trajectories (examples in **Supplementary Fig. 9**) for subsequent architectural measurements. To mitigate the non-uniform distribution caused by tract clustering in locally tractable regions, we used a farthest streamline sampling strategy[31] (**Fig. 2d**, **Supplementary Methods 3**) to achieve a uniform reconstruction throughout each compartment volume. Compared with unconstrained tracking, compartment constraints effectively suppressed boundary-crossing artifacts (**Fig. 4a**), enabling compartment-resolved fiber reconstruction and laying the foundation for finger-specific architectural measurement and functional assessment.

Anatomical validation of the muscle compartments

To confirm that the 3D volumes obtained by in vivo segmentation corresponded to the four

neuromuscular compartments of the FDS, rather than being spurious structures caused by imaging noise, registration error or passive deformation, we performed anatomical validation at both the level of macroscopic topology and microscopic fiber orientation. For this purpose, we assessed whether the relative spatial arrangement of compartments matched classic cadaveric descriptions, and whether fibers within each compartment exhibited continuous, physiologically interpretable trajectories[23, 32, 33].

At the macroscopic level, volumetric compartment masks reconstructed by the multimodal imaging framework showed a highly consistent spatial arrangement across participants and agreed with previously reported cadaveric spatial topology of the FDS (**Fig. 3a**). **Supplementary Movie 3** provides a rotating visualization along the proximal-to-distal forearm axis, illustrating how compartments are organized within the forearm contour. Specifically, segmentation reproduced the characteristic two-layer architecture, with the compartments controlling the middle and ring fingers located mainly in the superficial layer, the middle compartment more radial and the ring compartment more ulnar. The compartments controlling the index and little fingers were located primarily in the deep layer and likewise exhibited a radial-ulnar separation trend. These compartments were not merely stacked side by side within a cross-section. Instead, they maintained stable relative positions along both the superficial-deep and ulnar-radial dimensions. This consistency indicates that piecewise segmentation can extract anatomically meaningful compartment boundaries despite substantial muscle-belly overlap. Beyond the spatial topology, the relative compartment sizes were further numerically validated. The distributions of physiological cross-sectional area (PCSA) and volume fraction across compartments agreed between in vivo and anatomical data, preserving the same grouping patterns (**Fig. 4e**, PCSA: index $\approx$ middle > ring $\approx$ little; volume fraction: middle & ring > index & little). Collectively, these findings delineate a hierarchy within the FDS, characterized by a systematic size gradient where superficial and radial compartments predominate over their deeper and more ulnar compartments.

At the microscopic level, compartment-constrained tractography further supported the physiological validity of the segmented compartments. After tractography within the segmented volume masks, each compartment contained continuous, ordered fiber tracts rather than noise-driven disorganized streamlines (**Fig. 3b**). Orientation-coded tractography showed that in the index, middle and ring compartments, proximal fibers were generally more aligned with the forearm long axis and progressively tilted from ulnar to radial orientation distally along the muscle belly. In contrast, fibers in the little-finger compartment were more oblique overall, and their proximal

orientation was more tilted than in other compartments, consistent with shorter proximal fibers (**Fig. 3b**, Little). This compartment-specific pattern of fiber orientations was consistent across all ten participants (**Supplementary Fig. 10**) and in agreement with existing cadaveric descriptions of the FDS anatomy[23, 32], providing a validated basis for subsequent architectural measurements. This agreement also extended to fiber-level properties. Quantitatively, compartment fiber length (FL) ranked identically between in vivo and anatomical data (middle > ring > index > little), while pennation angle (PA) remained stable across compartments (average difference < 2°) with low inter-subject variability (standard deviation < 5°) in both datasets (**Fig. 4e)**. Altogether, these microstructural findings reveal an architectural pattern characterized by intra-compartment fiber homogeneity and a shorter fiber length within the deeper compartments (index and little).

Spatial projection of 3D compartments onto 2D skin surface for EMG validation

Based on the surface anatomy, we projected the reconstructed 3D compartments onto the 2D skin surface to construct subject-specific compartment boundaries, enabling spatial comparison between architecture (in vivo imaging) and function (electrical signals). We then overlaid these boundaries with activation maps recorded during individual-finger isometric contraction tasks (**Fig. 3c, Supplementary Movie 4**). We found that 95% (38/40) of EMG activation centers for the target finger lay within the projected boundary of the corresponding compartment. The middle and ring compartments showed 100% concordance, whereas the index and little compartments each had one deviation (both 90%). These results demonstrate, at the functional level, a consistent spatial concordance between the segmented compartments and finger-specific neural drive. These findings provide strong functional validation of the proposed imaging-based segmentation, showing that compartment boundaries reconstructed in vivo indeed accurately predicted the spatial focus of finger-specific myoelectric activity on the skin surface.

Backtracking the deviating samples on the MRI images (**Supplementary Fig. 11**) suggested that these deviations more likely reflected spatial 'pulling' caused by synergistic muscle co-contraction and volume-conductor effects, rather than systematic segmentation error. For example, during the little-finger task in some participants, co-contraction of neighboring palmaris longus or flexor carpi ulnaris could have generated electric potentials that shifted the composite center away from the FDS region, resulting in center displacement. This observation may help explain why deviations were concentrated in the index and little compartments.

Muscle architecture and finger-specific functional roles

We further measured the architectural properties of the FDS and its compartments. Compartment-constrained tractography confined fibers strictly within each compartment (**Fig. 4a**), preventing bias in architectural parameters caused by boundary-crossing tracts. For whole-muscle FDS architecture, parameters derived from segmented tracking were more consistent with anatomical references[23] (**Fig. 4c**). Difference analysis showed that unsegmented tracking introduced substantial errors in the estimates of FL and PCSA, which are two key functional parameters (**Fig. 4d**). Using segmented tracking, we compiled an in vivo architectural dataset from the ten participants across the four compartments (**Supplementary Table 1**). We provide representative in vivo images and fiber data for one representative participant in **Supplementary Data 1**. The distributions of compartment architectural parameters were broadly similar between in vivo measurements and the anatomical references (**Fig. 4e**).

The four compartments showed pronounced grouped differences in FL and PCSA, overall separating into an index–middle group and a ring–little group, indicating systematic differences in displacement capacity (related to FL) and force capacity (related to PCSA). Accordingly, we constructed a 2D functional space with PCSA and FL as axes (**Fig. 4f**). In this space, the four compartments formed an approximately rectangular distribution that reflects their relative force–displacement capabilities. The index compartment occupied the high-force/low-displacement quadrant, suggesting a greater role in generating grasp force. The middle compartment combined high force and high displacement capacity and had the highest power potential, implying a prominent role in both force and envelope generation during grasp. The ring compartment had low force but high displacement capacity, consistent with providing grasp envelope. The little compartment occupied the low-force/low-displacement quadrant with the lowest power capacity, suggesting limited independent output and greater reliance on synergistic mechanisms.

PCSA represents the effective cross-sectional area perpendicular to fiber orientation and reflects the number of fibers in parallel, and is therefore commonly used to predict maximum isometric force. To test this assumption, we measured maximum voluntary contraction (MVC) force for each finger and performed linear regression between MVC and the corresponding estimated compartment PCSA. PCSA and MVC separated the four fingers into two functional groups: the index–middle group had significantly higher PCSA and MVC than the ring–little group (**Supplementary Fig. 13**). However, at the individual finger level, the linear relationship between PCSA and MVC was not significant across participants. When pooling all fingers, MVC showed

a weak association with PCSA ($R^2 = 0.2354$, **Supplementary Fig. 14**). Thus, PCSA better captured inter-finger differences in force capacity, but did not explain inter-individual variability in individual-finger MVC.

Discussion

We presented a multimodal imaging framework that combines dynamic ultrasound annotation with a 3D anatomical MRI reference to achieve, for the first time, in vivo volumetric segmentation and precise architectural characterization of neuromuscular compartments in the human FDS. We rigorously validated these imaging-derived compartments both anatomically and functionally. By reconstructing 3D compartment-constrained fiber trajectories and measuring key architectural properties, our framework delivers the compartment-level ground truth required to build neuromechanical digital twins with substantially higher fidelity than previously possible.

Methodology of piecewise segmentation

The central assumption of compartment identification is that, during target-finger movement, the target compartment moves in a different direction from the other compartments. This assumption is supported by two lines of evidence. First, intramuscular fiber movement exhibits locally multidimensional directionality[19, 34]. Second, during contraction, active and passive components can have similar amplitudes but different directions[35]. Using direction rather than amplitude as the segmentation marker avoids amplitude ambiguity arising from the superposition of active and passive components. Ensuring direction specificity requires a controlled experimental condition in which the target finger moves voluntarily while the non-target fingers are passively constrained. This constraint mechanically limits movement in adjacent compartments and stabilizes movement independence by modulating sensory feedback[36]. Converging evidence from the movement trajectory (dominated by the target finger) (**Fig. 2a**) and the tissue direction field (distinguishable directions for the target compartment) (**Fig. 2c**) confirms the specificity of this experimental paradigm.

The region growing algorithm in the annotation stage combines the direction field with anatomical priors to generate compartment regions with minimal spatial overlap, in contrast to the overlapping activation areas reported by prior MRI approaches[26]. Seed point sampling experiments indicated low sensitivity to initial seed conditions (overlap > 0.95 for grown regions within the same compartment). In the registration stage, we first generated a uniformly dense set of feature points

within the FDS muscle contour via farthest point sampling. Then, we performed minimum-weight registration between the two imaging modalities based on the topological invariance of corresponding muscle points, using the sum of squared distances between point pairs as the energy metric to satisfy a minimum-energy criterion for muscular deformation. This registration to the MRI neutral position simultaneously corrected for differences in forearm posture and for deformations caused by ultrasound probe compression.

Validation with in vivo imaging and surface EMG

Because no gold standard exists for in vivo compartment segmentation, we constructed a two-tier evidence chain: macroscopic–microscopic anatomical plausibility and cross-modal functional concordance. At the macroscopic level, all ten participants consistently exhibited a two-layer FDS organization (superficial middle and ring, deep index and little) and the expected ulnar–radial separation of compartments, in close agreement with cadaveric descriptions[23, 33]. At the microscopic level, orientation-coded tractography showed continuous, ordered fiber trajectories within each compartment, with the little-finger compartment exhibiting overall oblique fibers and shorter proximal fibers. The anatomical plausibility was numerically validated based on the similarity of architectural properties to those of anatomical references, as these properties quantify macroscopic compartment size and microscopic fiber orientation. We note inherent limitations in comparing in vivo data with anatomical data due to postmortem morphological changes and subjectivity. The unavailability of living specimens means that a true in vivo gold standard cannot be obtained. Our cohort comprised Asian participants, which precludes assessment of potential population differences in little-finger compartment architecture. In Asian populations, the little-finger compartment tends to originate near the medial epicondyle and the tendon spans the entire compartment, whereas in other populations the tendon may split or be absent in the middle portion[32, 37]. All participants in this study were Asian and passed an independent little-finger flexion test, consistent with the anatomical characteristic of an intact little-finger tendon in Asian cohorts.

The spatial focus of myoelectric activity during finger-specific control was predicted within the reconstructed compartments, confirming functional concordance. The small deviations in the EMG-based validation can be attributed to the co-contraction of synergistic muscles adjacent to the FDS (for example, palmaris longus and flexor carpi ulnaris) and to volume conductor effects that spatially shift the center. The direction of the shift was consistent with co-activated wrist flexor

regions adjacent to the MRI-defined location, rather than indicating a systematic segmentation error. This, in turn, suggests that individual-finger decoding from surface EMG is readily affected by crosstalk from neighboring regions. Unlike previous studies that compared modalities qualitatively along image intersection lines[28, 38], our approach projects ultrasound into the MRI coordinate system, enabling quantitative validation of anatomical boundaries against EMG centers across the entire muscle length on the skin surface.

Compartment-resolved architecture reveals finger-specific functional specialization

Using compartment masks as anatomical constraints for tractography had a pronounced impact on FDS architectural measurement. Segmentation reduced FL and increased PCSA by ~29%, because compartment boundaries correctly terminated fiber propagation that would otherwise cross anatomical boundaries. The errors of FL and PCSA are linked, because PCSA is calculated from FL (see PCSA formula in "Computation of architectural parameters"). The segmented values were more consistent with cadaveric references, confirming that compartment masks captured meaningful anatomical boundaries. If only whole-muscle FDS architecture is required, the cost of segmentation may not be justified, because mean differences in the 20–30% range can be coarsely estimated. However, explicit segmentation is still an indispensable prerequisite for compartment-level modelling.

Besides improving the measurement of the FDS muscle, the compartment-level measurement, in turn, revealed architectural differences among the four compartments that illuminate the respective functional roles of the fingers. In the force–displacement functional space defined by PCSA and FL, the four compartments separated into two functional groups, including the index–middle group (high force capacity) and the ring–little group (low force capacity), consistent with clinical observations[25]. The former provides the main power for grasp, whereas the latter contributes enclosure and stabilizing assistance. PCSA can capture MVC differences via the weak linear relationship between PCSA and MVC across fingers, but it cannot predict inter-individual variability in MVC for a specific finger. This weak association reflects the fact that PCSA is not the sole determinant of maximal isometric force, and the force also depends on factors such as pennation angle, tendon slack length and neural recruitment capacity[31].

Implications of in vivo architecture for neuromechanical investigations, computational models, and interfacing

Beyond revealing finger-specific functional roles, this compartment-resolved architecture provides a missing anatomical substrate for fundamental neuromechanics research. Knowing the precise 3D extent and fiber organization of each compartment enables targeted recording of their neural drive. For example, intramuscular electrode arrays[39] can now be targeted to sample motor units from specific compartments, allowing, for the first time, the systematic study of motor neuron synergistic control at the level of a single digit and during multi-finger hand tasks. This creates a direct bridge between the conceptual framework of functional motor neuron clusters and their mechanical outputs at the compartment level[15].

These architectural properties and fiber trajectories have direct value for computational modelling and support the feasibility of subject-specific modelling. For musculoskeletal models, compartment-specific data can replace scaled values used when measured data are unavailable[18, 40], particularly for force-sensitive parameters such as FL and PCSA[19]. For EMG modelling, the 3D fiber trajectories reconstructed under compartment constraints can replace the common curved-fiber assumption of constant length[20, 21, 41]. Digital-twin studies of EMG indicate that fiber number, depth, mediolateral position, innervation zone and FL are among the most sensitive parameters[41], all of which can be derived from the proposed reconstructed fiber trajectories. This highly detailed architectural information provides a path toward subject-specific neuromechanical and biophysical digital twins[13, 21], which may in turn be crucial for data augmentation and performance optimization in neuromuscular interfaces based on wearable devices[14].

The value of compartment mapping extends to neuromuscular interfaces. Skin-surface projections of compartment boundaries revealed extensive inter-compartment overlaps (**Fig. 3c**), raising the question of how such overlaps affect neural-interface decoding. As a preliminary analysis of this issue, we incorporated compartment anatomy into channel optimization for individual-finger flexion force estimation (the details of this analysis are in **Supplementary Note 1, Movie 5**). The results indicated that anatomical overlap limits the benefit of finger-specific channel selection, providing a structural explanation for the long-standing difficulty of isolating finger-specific EMG signals from the forearm surface. More broadly, this and other classic challenges in EMG analysis and interpretation may be addressed by combining the highly accurate anatomical and architectural information delivered by our multimodal imaging framework with future advances in inverse EMG modelling, in which activation and related parameters are estimated by inverting the transfer

function of a volume conductor derived from a neuromuscular digital twin.

Limitations

Some limitations should be noted. First, the cohort comprised 10 right-handed Asian participants (8 male, 2 female). This relatively small sample size and sex imbalance limit generalizability and preclude testing the variability across ethnic groups, particularly for the little-finger compartment. Nevertheless, the proposed framework is not tailored to this specific cohort and should be directly applicable to broader populations. We see no sample-specific factors that would plausibly limit its validity or feasibility in other groups. In the same way, the chosen FDS muscle can be considered as a representative application of the multimodal imaging methods introduced in this study. The same framework can indeed be applied to other body parts, such as the lower limb or trunk.

Second, because compartments are defined functionally, residual co-contraction[25] and the current long-axis sampling density constrain segmentation fidelity and volumetric resolution. Third, validation relied on surface EMG, whose limited depth sensitivity and volume-conductor effects may reduce sensitivity to deep activity, although MRI indicates that FDS depth in our participants was within the typical detection range of 30 mm[42].

Conclusion

We achieved in vivo multimodal mapping of finger-specific neuromuscular compartments in the human FDS by combining ultrasound and MRI for volumetric segmentation and compartment-constrained tractography. The segmentation was supported by anatomical plausibility and a close spatial match between compartment projections and EMG activation centers. These compartment-resolved architectures and trajectories provide key inputs for physiological computational models, making realistic, finger-specific biomechanics and EMG simulations feasible.

Materials and Methods

Participants

Ten healthy right-handed participants (8 men, 2 women, age 25 ± 3 years, body mass index 24 ± 3 kg/m²) completed MRI, ultrasound and EMG experiments. Inclusion criteria were no upper-limb musculoskeletal disorders, peripheral nerve injury, other neurological disease, or relevant trauma

history. All participants provided written informed consent before the experiments. The study protocol was approved by the institutional ethics committee and conducted in accordance with the Declaration of Helsinki.

Imaging protocols and multimodal acquisition

We designed and implemented multimodal acquisition protocols combining MRI and ultrasound.

a) MRI. The scans were performed on a 3.0 T whole-body scanner (MAGNETOM Prisma, Siemens Healthcare, Erlangen, Germany) with a gradient system of maximum gradient strength 80 mT/m and maximum slew rate 200 T/m/s. Signal reception used an 18-channel flexible body coil array to accommodate forearm geometry. Participants lay supine with the forearm relaxed in a neutral position, fixed in a customized MRI-compatible device to reduce involuntary movement and avoid compression-induced deformation (**Supplementary Fig. 3**). We acquired two key sequences (raw images in **Supplementary Fig. 1**).

Anatomical reference sequence: we used a simultaneous multi-slice T2-weighted turbo spin echo sequence with the following parameters: field of view = 120 × 120 × 282 mm^3, acquisition matrix = 448 × 448, number of slices = 94, voxel resolution = 0.27 × 0.27 × 3 mm^3, repetition time/echo time = 3500 ms/39 ms, total scan time = 3 min 36 s.

Fiber tractography sequence: we acquired a readout-segmented diffusion tensor imaging sequence with the following parameters: field of view = 102 × 130 × 260 mm^3, acquisition matrix = 80 × 160, number of slices = 34, voxel resolution = 3 × 1.6 × 1.6 mm^3, repetition time/echo time = 5500 ms/69 ms. Diffusion weighting was b = 400 s/mm^2 with 12 non-collinear gradient directions, plus four b = 0 s/mm^2 reference images. Spectral fat suppression and parallel imaging (acceleration factor 2) were used. Total scan time was 4 min 52 s.

Diffusion tensor imaging preprocessing used the b = 0 image as the reference and applied FSL 6.0[43] to correct eddy-current distortions, movement artifacts and susceptibility effects. We then denoised the data using local principal component analysis filtering[44]. To obtain anatomical constraints, we performed piecewise registration of the diffusion tensor imaging to the T2-weighted images[45]. The registration achieved coarse axial alignment using surface markers (vitamin D capsules placed around the wrist and elbow[46], **Supplementary Fig. 2**), then partitioned the volume into ~15 axial segments and applied affine transformations to each segment for refined alignment. Diffusion gradient directions were adjusted accordingly via b-matrix rotation[47].

Using the T2-weighted anatomical images, we manually segmented the FDS in ImageJ[48] to generate a muscle mask, with cubic-spline interpolation between slices. This mask served as the region of interest (ROI) for compartment segmentation and tractography, and as a spatial reference for ultrasound and EMG acquisition (**Supplementary Fig. 2**). Ultrasound and EMG acquisition sites were defined based on relative distances between wrist and elbow anatomical landmarks.

b) Ultrasound imaging. B-mode ultrasound was acquired using a programmable Vantage-256 research system (Verasonics Inc., Kirkland, Washington, United States) with a 128-channel linear array probe (L11-5v, center frequency 7.7 MHz). To capture contraction dynamics, we used plane-wave imaging at 500 Hz. The transverse field of view covered a depth of 40.0 mm and width of 38.0 mm, with axial and lateral resolutions of approximately 0.2 mm and 0.3 mm, respectively.

Participants were seated with the upper limb positioned on a custom experimental platform (**Fig. 2a**). The probe was translated along the forearm long axis at 3 cm intervals and fixed at each position to prevent relative slip. To maximize the movement of the target compartment and reduce co-contraction, all non-target fingers were restrained during acquisition. Guided by a metronome, participants performed 10 s of cyclic flexion of the target finger (1 Hz or 60 beats/min) while a data glove recorded and normalized proximal interphalangeal joint angles. The Verasonics system recorded raw radiofrequency signals, which were reconstructed into B-mode images via in-phase and quadrature demodulation and delay-and-sum beamforming. Imaging and preprocessing ensured adequate spatiotemporal resolution and data quality[49], providing a high-fidelity basis for subsequent compartment annotation. Preprocessing, segmentation and architectural analyses were performed using in-house Python utilities[31].

Piecewise segmentation

To address the challenge that conventional static MRI cannot distinguish neuromuscular compartments of the FDS, we proposed a strategy named piecewise segmentation (**Fig. 2b**). This strategy extracts compartment contours elicited by isolated finger movements from ultrasound and maps compartment contours to the 3D anatomical MRI space. Volumetric compartment masks are then generated by lofting (**Fig. 2c**).

The core hypothesis of piecewise segmentation is that, when non-target fingers are passively constrained and movement is dominated by the target finger[50], the movement direction of the target compartment is distinguishable from that of other compartments[19, 34]. We therefore prioritized movement direction rather than displacement magnitude to avoid amplitude ambiguity due to the

superposition of active and passive components[35]. Before segmentation, we manually delineated the outer contour of the FDS in both ultrasound and MRI images in ImageJ[48]. All subsequent annotation, matching and volume reconstruction were performed within this ROI contour to enforce consistent anatomical boundary constraints across modalities.

a) Ultrasound annotation. We performed semi-automated annotation on ultrasound image sequences acquired during isolated finger movement tasks (1 Hz flexion) to extract compartment contours corresponding to each finger.

Direction field estimation: we first applied the Farneback dense optical flow algorithm[51] to compute pixel-wise movement vectors for each frame of the ultrasound sequence. To obtain the dominant movement direction during the task, we integrated the vector field over time and normalized it to generate a tissue direction field corresponding to a specific finger movement. This direction field reflects the mean movement direction of each pixel during the task and reveals directional differences among compartments. The Farneback method is based on an approximate brightness-constancy assumption between consecutive frames. Formally, the brightness constancy can be expressed as:

$$f_2(x) = f_1(x + \boldsymbol{d}) \quad <1>$$

$f(x)$: brightness at a pixel x , and $\boldsymbol{d}$: displacement, represented by magnitude and direction. The displacement was obtained by fitting a polynomial expansion under the brightness-constancy assumption. The Farneback method was implemented with a pyramid scale of 0.7, 3 levels, and a 30-pixel window, followed by Gaussian smoothing (σ =7.0) within the ROI of FDS to enhance spatial coherence and noise robustness.

Region extraction: based on the direction field, we used a region growing algorithm (**Supplementary Methods 1**) for segmentation. We first defined a preset region for each compartment according to the tissue movement direction field (**Fig. 2c**) and anatomical priors (**Fig. 3a**), and placed two seed points within this region via farthest point sampling. Region growing was performed for each seed pair, and growth results within the preset region were merged to obtain the target compartment region. Starting from the seed points, region growing iteratively added 8-connected neighborhood pixels based on direction similarity until no pixels satisfied the threshold. The procedure is formally defined as follows:

$$\text{If } g(x,y) < t \Rightarrow y \in \boldsymbol{X} \quad <2>$$

$g(x,y)$: similarity metric between pixels, x : a pixel in the current segmented region, y : a candidate pixel in the 8-connected neighborhood of x , and t : similarity threshold. The similarity metric is defined as follows.

$$g(x,y) = \angle(\boldsymbol{m},\boldsymbol{n}) < t \quad <3>$$

$$t = a_{\max}(1-r) + a_{\min} r \quad <4>$$

$$r = d(q,y) / \sqrt{A/\pi} \quad <5>$$

$\boldsymbol{m}$: mean direction vector of the current segmented region, updated iteratively during growth, $\boldsymbol{n}$: direction vector at the candidate pixel y , t : dynamic angular (similarity) threshold, $a_{\max} = 30°$, $a_{\min} = 5°$: upper and lower angular bounds, r : angular scaling factor, $d(q,y)$: Euclidean distance between the seed point q and the candidate pixel y , and $\sqrt{A/\pi}$: radius of the equivalent circle of FDS muscle area A in the ultrasound cross-section. The dynamic angular threshold t increased as d decreased, prioritizing pixel inclusion near the seed point. This design reflects that the seed point was placed according to anatomy (**Fig. 3a**) and the direction field. The seeds were theoretically within the target compartment, and pixels distant from the seeds were more likely to belong to non-target compartments, consequently leading to termination of outward growth. No more than two seed points were placed per compartment, reflecting directional coherence within the target compartment. The segmented regions exhibited distinct spatial distributions across compartments.

To assess sensitivity to initialization, we varied seed point positions at 1 mm intervals within the anatomical preset region (**Supplementary Fig. 5-8**). The resulting grown regions overlapped by >0.95, indicating that the annotation strategy is robust to initial conditions.

b) Registration from ultrasound to MRI. Mapping multi-slice 2D ultrasound contours into the 3D MRI anatomical space is essentially a cross-modal alignment problem that must preserve topological continuity in the presence of deformation[29]. We performed registration using a minimum-energy matching strategy that uses the FDS outer contour as a bridge.

Uniform feature point sampling: on each corresponding cross-section, we performed farthest point sampling[52] within the ROI contour of FDS in both ultrasound and MRI to extract spatially uniform feature points, avoiding overly sparse features and improving registration stability. The sampling iteratively selects the candidate point farthest from the current point set, producing a point set with optimal spatial uniformity in the 2D domain until a predefined number of points is

reached (10,000 in this study). The next sampling point s_F is defined as follows:

$$s_F = \arg\max(\min_{p \in \boldsymbol{P} \setminus \boldsymbol{S}} d(p,s)) \quad <6>$$

$\boldsymbol{S}$: sampled point set, $\boldsymbol{P}$: set of all points, $\boldsymbol{P} \setminus \boldsymbol{S}$: unsampled point set, and $d(p,s)$: Euclidean distance between points p and s. The farthest point strategy ensures uniformity by maximizing the minimum distance between consecutive points. Geometrically, each subsequent point lies at the center of the largest empty region.

Minimum-energy matching: points uniformly distributed along the contour should maintain one-to-one correspondence between the two images. From a topological perspective, such correspondence arises from the topological invariance of muscle structure under continuous deformation. To establish one-to-one correspondences between modalities, we treated the sampled points from ultrasound and MRI as vertices on the two sides of a bipartite graph, with edge weights defined as squared Euclidean distances between candidate point pairs. By solving the minimum-weight perfect matching problem, we minimized the sum of squared distances of all matched pairs, achieving cross-modal minimum deformation energy and spatial continuity under the topological invariance assumption[53].

$$\boldsymbol{M}_W = \arg\min \sum_{(u \in \boldsymbol{U}, v \in \boldsymbol{V})} d^2(u,v) \quad <7>$$

$\boldsymbol{M}_W$: minimum weight matching (a bipartite graph matching approach), formulated on point pairs (10,000 points obtained from farthest point sampling), and $d^2(u,v)$: squared Euclidean distance between sampled points from the ultrasound image $\boldsymbol{U}$ and the MRI image $\boldsymbol{V}$.

The bipartite matching operates directly on the coordinates of the two images. Under the topological invariance assumption, coordinate-system transformations do not affect the matching.

Contour mapping (Supplementary Methods 2): based on the established correspondences, we mapped compartment contour points in the ultrasound image into the MRI coordinate system. For each contour point, we located its nearest sampled point in the ultrasound point set and transferred it to the matched MRI point location, thereby obtaining compartment contours in MRI coordinates.

c) 3D lofting in MRI. Compartment contours obtained from different cross-sections were interpolated along the muscle long axis using smoothed cubic splines[54] to generate 3D volumetric masks for the four compartments, which served as ROI constraints for subsequent tractography.

Because contours acquired in MRI reflect anatomical boundaries in a relatively neutral posture,

the minimum-energy matching process can partially correct for differences in forearm posture and deformation induced by ultrasound probe compression[18]. Robustness to muscle deformation is illustrated in **Supplementary Movie 2**, which shows compartment movement during finger movement.

Fiber tractography

To reconstruct the fiber tracts from diffusion tensor imaging, we performed deterministic tractography[31] under anatomical constraints defined by each volumetric compartment mask, and used the derived streamlines for subsequent computation and visualization of architectural parameters (**Fig. 4b**).

a) Tensor data extraction. We estimated diffusion tensors in DSI Studio (version 2023)[55] by fitting a second-order diffusion tensor model in each voxel to obtain eigenvalues and eigenvectors, where the principal eigenvector represents the local dominant fiber orientation. Fractional anisotropy was extracted to set tracking thresholds. For spatial normalization, both masks and diffusion tensor imaging data were resampled to 1 mm isotropic resolution[31].

b) Uniform fiber reconstruction under anatomical constraints. We used four volumetric masks of the FDS compartments as anatomical boundaries. Seeding was restricted to within each mask, and streamline propagation was terminated when a streamline reached the mask boundary or exited the mask[54], thereby suppressing inter-compartment artifacts (as shown in **Fig. 4a**).

Deterministic tractography and post-processing[31]: streamlines were propagated bidirectionally along the principal eigenvector with a step size of 1 mm. Tracking was terminated when fractional anisotropy < 0.1, curvature $> 20°$ or the streamline exited the compartment mask. Streamlines shorter than 10 mm were removed, and remaining fibers were smoothed by third-order polynomial fitting to obtain physiologically plausible 3D curvature.

In this study, the terms “fiber tracts” and “streamlines” are used interchangeably to denote the reconstructed trajectories, except where density quantification requires distinction. Streamline distributions are typically interpreted under an assumption of uniform fiber density in biological tissues. To reduce non-uniform streamline distributions such as clustering in regions with high anisotropy or sparse discontinuities near fascia, we introduced farthest streamline sampling in our previous work[31] (**Supplementary Methods 3**). Similar to the farthest point sampling used in compartment annotation, farthest streamline sampling replaces points with streamlines. The method minimizes preferential sampling of clustered or long streamlines and instead generates the

next streamline in the largest empty region, promoting uniform spatial coverage. Specifically, we first generated 10,000 candidate streamlines within each mask, then iteratively selected the candidate streamline farthest from the sampled set according to a streamline distance metric until a uniformly distributed subset was obtained (3,000 streamlines)[40]. All subsequent architectural measurements were based on this uniform subset.

Computation of architectural parameters

We computed six architectural parameters from the volumetric masks and reconstructed fiber tracts (**Fig. 4b**): muscle volume (MV), fiber length (FL), muscle length (ML), FL/ML ratio, pennation angle (PA) and PCSA. These architectural properties are important in anatomy and musculoskeletal modelling[17]. For example, FL and PCSA can quantify the force and displacement capacity.

1. MV was determined by summing the voxel volumes within the compartment mask:

$$MV = N \cdot V \quad <8>$$

where N is the number of voxels in the compartment mask and V is the physical volume of a single voxel.

2. FL of a single streamline was defined as the integrated length of the reconstructed streamline, computed by summing Euclidean distances between adjacent points. FL relates to the displacement capacity of muscle[40].

3. PA of a streamline was defined as the angle between the orientation at the two streamline endpoints and the muscle line of action[56]. The line of action was estimated as the average orientation across all streamlines. Although the line of action can be defined more precisely based on muscle architectural type[56], this is computationally complex and the difference has been shown to be small. For each muscle or compartment, FL and PA were represented by the median across all streamline measurements (see "Statistical analysis").

4. ML was defined as the distance between the most distal and most proximal points along the line of action.

5. FL/ML ratio is an intrinsic, scale-invariant property that facilitates comparisons across participants and across studies.

6. PCSA represents the total muscle cross-sectional area perpendicular to the fiber orientation. We

computed PCSA using the classical formula[40]:

$$PCSA = MV \cdot \cos(PA) / FL \quad <9>$$

By combining FL (related to displacement capacity) and PCSA (related to force capacity)[40], we constructed the architecture-based 2D functional space for the fingers shown in **Fig. 4f**.

Except for ML and the FL/ML ratio, we computed MV, FL, PA and PCSA for each compartment. Compartment volume fraction is an intrinsic property and was expressed as the percentage of each compartment volume relative to the total muscle volume. We compared compartment architectural parameters with anatomical references[23]. In addition, we calculated FDS architectural parameters between segmented and unsegmented conditions by using either the union of all compartment masks or only the whole FDS mask as the tractography termination boundary. We compared the segmented, unsegmented and anatomical[32] FDS architectures. In principle, segmented architectural properties should be closer to anatomical values because compartment masks correctly define anatomical constraints that terminate fiber propagation.

EMG acquisition

We built an EMG experimental platform that synchronously recorded high-density surface EMG and finger forces (**Supplementary Fig. 4, Movie 4**). The platform supported EMG-based validation of functional concordance by aligning high-density surface EMG activation spatial distributions with imaging-based compartment boundaries.

a) Data acquisition and experimental setup. EMG signals were recorded using a 64-channel high-density surface EMG system (Quattrocento, OT Bioelettronica, Turin, Italy). Skin preparation included shaving, abrasion and alcohol cleaning, and conductive paste was applied to reduce electrode–skin impedance. The reference electrode was placed near the ulnar styloid. EMG was recorded in monopolar mode with a gain of 150, analog hardware bandpass filtering 10–4400 Hz, sampling rate 2048 Hz, and 16-bit analog-to-digital conversion. Offline, signals were bandpass filtered (20–500 Hz, fourth-order Butterworth) and a comb filter was used to remove 50 Hz power-line interference[42]. To reduce the influence of onset/offset transients on amplitude estimation, the first and last 1 s of each trial were discarded. Individual-finger flexion force was measured using a mechanical force gauge (SanLiang, NK Series, China). Before experiments, we measured the MVC of flexion for each finger except the thumb. The target finger was connected to the force gauge. Other fingers remained extended, and participants were instructed to minimize involuntary

contraction. Participants performed individual-finger isometric flexion at 25% MVC for 12 s/trial.

b) Signal processing. We extracted the conventional RMS amplitude feature. RMS envelopes were computed for each channel using a 200 ms sliding window with a 50 ms step, capturing electrical activity intensity with a balance between temporal resolution and stability. Channel RMS values were normalized to 0–1, and RMS was averaged across three repeated trials under the same condition. This average RMS was used to construct activation maps for EMG-based validation.

Electrodes were placed on the muscle belly surface parallel to the FDS long axis (**Supplementary Fig. 2, 4**). Two flexible electrode grids were used (13 × 5 layout, electrode diameter 1 mm, inter-electrode distance 8 mm). The center $\bar{x}$ of the surface EMG map was defined as a weighted average position and used to assess the spatial distribution of muscle activity or activation[42]. Activation centers were computed from normalized RMS activation maps to localize the spatial position of dominant activation from the target finger.

$$\bar{x} = \sum_{i=1}^{n} (r_i \cdot x_i) / \sum_{i=1}^{n} r_i \quad <10>$$

x_i : coordinate point in the electrode coordinate system (n points in total), and r_i : RMS value at x_i. Coordinates with RMS > 0.8 were used to compute the center to enhance sensitivity to the activated areas.

To validate segmentation using subject-specific data, we projected 3D anatomical architecture onto the skin surface based on surface anatomy concepts, enabling comparison of the spatial consistency of compartments in terms of architecture and functional electrical signals. We identified electrode-surface voxels within the MRI-derived forearm mask according to electrode position and size, and used the mean surface normal of the electrode surface as the projection direction to project the segmented compartment boundaries onto the electrode surface. Because the EMG signals during a target-finger task should arise within the corresponding compartment, we compared the projected boundaries with the activation center of the RMS activation map. If the center fell within the projected boundary of the corresponding compartment, the sample was considered to pass the functional concordance test. Accuracy was defined as the fraction of centers falling within the boundaries.

Data quality

To ensure reliability of multimodal data, we implemented quality-control procedures across data acquisition, experimental setup and signal preprocessing.

a) MRI quality. An MRI-compatible device fixed the forearm to reduce involuntary movement. The mean signal-to-noise ratio[57] of T2-weighted anatomical images was 40 ± 9, indicating high anatomical clarity. Diffusion-weighted image quality was reflected by the b = 0 images, with mean signal-to-noise ratio of 26 ± 3. Diffusion imaging parameters, including signal-to-noise ratio, b-value selection and number of diffusion directions, met standards for reliable skeletal-muscle diffusion tensor fitting and tractography[58]. We initially recruited 12 participants and 2 were excluded due to obvious movement artifacts, leaving 10 participants with acceptable data quality. Given reports that ~20% of individuals may congenitally lack the FDS little-finger tendon[23], we performed functional screening before ultrasound experiments. With the index, middle and ring fingers fixed and extended, participants were asked to flex the proximal interphalangeal joint of the little finger independently[22] to exclude anatomical variations that could affect independent little-finger control. No participants failed this test.

b) Ultrasound imaging quality. Conventional line-by-line focused beam scanning typically achieves frame rates of 30–60 Hz and is insufficient to capture transient deformation during muscle contraction[28]. We used plane-wave imaging to increase the frame rate to 500 Hz, ensuring that inter-frame displacement remained sub-pixel during the 1 Hz finger-flexion task, thereby eliminating temporal aliasing and enabling continuous, accurate movement estimation.

The fascia of the FDS appears as a hyperechoic band in ultrasound images. By reconstructing images using delay-and-sum beamforming on raw radiofrequency data, we achieved an axial resolution of ~0.2 mm and lateral resolution of ~0.3 mm. This resolution facilitates identification of fascia with a thickness of ~0.5–1.0 mm, allowing compartment segmentation to be confined within the anatomical boundary of the FDS muscle.

Probe sliding or compression relative to the skin can cause geometric distortion, and out-of-plane movement[29] can affect alignment between 2D ultrasound slices and 3D MRI slices. The probe was fixed on a custom platform with multi-degree-of-freedom adjustment rails (**Fig. 2a**) to prevent jitter and relative movement from handheld operation. The platform also restricted forearm pronation and supination to ensure that acquisition planes remained perpendicular to the muscle long axis, reducing out-of-plane signal loss due to muscle twisting. Finger constraint and metronome guidance further reduced movement artifacts induced by non-target fingers.

c) EMG quality. During preprocessing, RMS was computed for each channel. Channels whose RMS exceeded the mean ± 3 standard deviations across all channels were classified as abnormal and removed. All EMG experiments were repeated three times, and the three trials were averaged

for analysis to reduce random variability from single acquisitions.

Statistical analysis

Normality was assessed using the Shapiro–Wilk test. We used the median values across all streamlines as the representative value for each muscle or compartment[40], because FL and PA of streamlines followed a non-normal distribution within a given muscle volume (**Supplementary Fig. 12**). Architectural properties across the subjects followed a normal distribution and are therefore reported as mean ± standard deviation.

Statistical analyses were conducted in IBM SPSS Statistics 25 with a significance level $\alpha = 0.05$. Greenhouse–Geisser correction was applied when the sphericity assumption was violated. Comparisons of architectural parameters between compartments and between segmentation conditions used paired t-tests with Bonferroni correction. We used box plots to present the architectural data alongside anatomical reference, and applied one-sample t-tests to assess whether PA and FL/ML ratio fell within known physiological ranges (PA < 10° for FDS and its compartments, FL/ML ratio = 0.2–0.6 for FDS[31]). The architectural data fell within the physiological ranges.

Ethics

All experiments involving human participants were approved by the Institutional Review Board for Human Research Protections of Shanghai Jiao Tong University (No. E2021178C and E20240248I). Each participant provided written informed consent.

Acknowledgements

This work was supported in part by the National Natural Science Foundation of China under Grants 52227808 and 52575026. We thank the support from Siemens Healthineers Ltd.

Author contributions

Y.L. and Y.Y. conceived the idea and designed the study. Y.L., Y.Y., Y.K., Z.Y., S.M., Y.W. and Q.L. performed the data collection. Y.L., Y.Y., Y.K. and D.F. analyzed and interpreted the results. Y.L. wrote the original manuscript. X.J., D.F. and X.Z. directed the project. All the authors contributed to the writing and editing.

Competing interests

The authors declare no competing interests.

Data availability

The muscle compartment data of a representative subject are provided in **Supplementary Data 1**, including T2-weighted images, diffusion-weighted images, and fiber tracts from tractography.

References

1. Xu J, Mawase F, Schieber MH. Evolution, biomechanics, and neurobiology converge to explain selective finger motor control. *Physiol Rev* **104**, (2024).

2. Madarshahian S, Letizi J, Latash ML. Synergic control of a single muscle: The example of flexor digitorum superficialis. *Journal of Physiology-London* **599**, 1261-1279 (2021).

3. Osswald M, Cakici AL, de Oliveira DS, Braun DI, Farina D, Del Vecchio A. Task-specific motor units in the extrinsic hand muscles control single- and multidigit tasks of the human hand. *J Appl Physiol* **138**, 1187-1200 (2025).

4. Mariappan YK, Manduca A, Glaser KJ, Chen J, Amrami KK, Ehman RL. Vibration imaging for localization of functional compartments of the extrinsic flexor muscles of the hand. *J Magn Reson Imaging* **31**, 1395-1401 (2010).

5. Heckman CJ, Enoka RM. Motor Unit. *Comprehensive Physiology* **2**, 2629-2682 (2012).

6. Farina D*, et al.* Toward higher-performance bionic limbs for wider clinical use. *Nat Biomed Eng* **7**, 473-485 (2023).

7. Roy R, Sprague AH, Shahrooei A, Hu X, Kamper D. Reliability of individual finger force prediction from electromyographic signals recorded from surface arrays: Implications for assistive device use. *J Neural Eng* **23** (2026).

8. Losanno E, Mender M, Chestek C, Shokur S, Micera S. Neurotechnologies to restore hand functions. *Nature Reviews Bioengineering* **1**, 390-407 (2023).

9. Crema A, Malesevic N, Furfaro I, Raschella F, Pedrocchi A, Micera S. A Wearable Multi-Site System for NMES-Based Hand Function Restoration. *IEEE Trans Neural Syst Rehabil Eng* **26**, 428-440 (2018).

10. van Beek N, Stegeman DF, van den Noort JC, Veeger D, Maas H. Activity patterns of extrinsic finger flexors and extensors during movements of instructed and non-instructed fingers. *J Electromyogr Kinesiol* **38**, 187-196 (2018).

11. Gao Z*, et al.* Extensor Digitorum Communis Compartments With a Double Compensation Synergy Strategy for Constant Force Control of the Index Finger. *IEEE Trans Neural Syst Rehabil Eng* **31**, 1451-1461 (2023).

12. Zatsiorsky VM, Li ZM, Latash ML. Enslaving effects in multi-finger force production. *Exp Brain Res* **131**, 187-195 (2000).

13. Farina D, Merletti R, Enoka RM. The extraction of neural strategies from the surface EMG: 2004-2024. *J Appl Physiol* **138**, 121-135 (2025).

14. Kaifosh P*, et al.* A generic non-invasive neuromotor interface for human-computer interaction. *Nature* **645**, (2025).

15. Hug F, Avrillon S, Ibanez J, Farina D. Common synaptic input, synergies and size principle: Control of spinal motor neurons for movement generation. *Journal of Physiology-London* **601**, 11-20 (2023).

16. Petersen E, Rostalski P. A Comprehensive Mathematical Model of Motor Unit Pool Organization, Surface Electromyography, and Force Generation. *Front Physiol* **10**, (2019).

17. Charles JP, Grant B, D'Aout K, Bates KT. Subject-specific muscle properties from diffusion tensor imaging significantly improve the accuracy of musculoskeletal models. *J Anat* **237**, 941-959 (2020).

18. Verheul J, Yeo S-H. A hybrid method for ultrasound-based tracking of skeletal muscle architecture. *IEEE Trans Biomed Eng* **70**, 1114-1124 (2023).

19. Valero-Cuevas FJ, Cohn BA, Yngvason HF, Lawrence EL. Exploring the high-dimensional structure of muscle redundancy via subject-specific and generic musculoskeletal models. *J Biomech* **48**, 2887-2896 (2015).

20. Robertson JW, Johnston JA. Modifying motor unit territory placement in the Fuglevand model. *Med Biol Eng Comput* **55**, 2015-2025 (2017).

21. Maksymenko K, Clarke AK, Mendez Guerra I, Deslauriers-Gauthier S, Farina D. A myoelectric digital twin for fast and realistic modelling in deep learning. *Nat Commun* **14**, (2023).

22. McIsaac TL, Fuglevand AJ. Motor-unit synchrony within and across compartments of the human flexor digitorum superficialis. *J Neurophysiol* **97**, 550-556 (2007).

23. Campisi ES, Johnston M-L, Kelly EC, Tran J, Switzer-McIntyre S, Agur AMR. Intramuscular aponeuroses and fiber bundle morphology of the five bellies of flexor digitorum superficialis: A three-dimensional modeling study. *J Anat* **242**, 1003-1011 (2023).

24. Fang C, Peternel L, Seth A, Sartori M, Mombaur K, Yoshida E. Human Modeling in Physical Human-Robot Interaction: A Brief Survey. *IEEE Rob Autom Lett* **8**, 5799-5806 (2023).

25. Li S, Latash ML, Yue GH, Siemionow V, Sahgal V. The effects of stroke and age on finger interaction in multi-finger force production tasks. *Clin Neurophysiol* **114**, 1646-1655 (2003).

26. Mariappan YK, Glaser KJ, Ehman RL. Magnetic resonance elastography: a review. *Clin Anat* **23**, 497-511 (2010).

27. Hojo E*, et al.* MR elastography-based slip interface imaging (SII) for functional assessment of myofascial interfaces: A feasibility study. *Magn Reson Med* **92**, 676-687 (2024).

28. Sheng Z, Bedoy E, Dicianno BE, Weber DJ, Kim K. Image-Derived Skeletal Muscle Activation Metric Map: A Forearm Study Using Ultra-Fast Ultrasound Imaging and High-Density Electromyography. *IEEE Trans Biomed Eng* **72**, 24-34 (2025).

29. Akhlaghi N*, et al.* Real-Time Classification of Hand Motions Using Ultrasound Imaging of Forearm Muscles. *IEEE Trans Biomed Eng* **63**, 1687-1698 (2016).

30. Zheng Y-P*, et al.* A reliability and validity study for Scolioscan: a radiation-free scoliosis assessment

system using 3D ultrasound imaging. *Scoliosis and Spinal Disorders* **11**, (2016).

31. Li Y, Ma S, Zhao J, Li Q, Sheng X. Optimized Uniform Sampling and Validation of Fiber Tracts From Magnetic Resonance Tractography for In Vivo Architectural Measurement of Human Forearm Muscles. *IEEE Trans Biomed Eng* **71**, 3370-3382 (2024).

32. Matsuzawa K, Edama M, Ikezu M, Kaneko F, Hirabayashi R, Kageyama I. The origin structure of each finger in the flexor digitorum superficialis muscle. *Surg Radiol Anat* **43**, 3-10 (2021).

33. Erguen S*, et al.* Old name, new face: A systematic analysis of flexor digitorum superficialis muscle with chiasma antebrachii. *Annals of Anatomy-Anatomischer Anzeiger* **247**, (2023).

34. Zhou G-Q, Zheng Y-P. Automatic fascicle length estimation on muscle ultrasound images with an orientation-sensitive segmentation. *IEEE Trans Biomed Eng* **62**, 2828-2836 (2015).

35. Englund EK, Elder CP, Xu Q, Ding Z, Damon BM. Combined diffusion and strain tensor MRI reveals a heterogeneous, planar pattern of strain development during isometric muscle contraction. *American Journal of Physiology-Regulatory Integrative and Comparative Physiology* **300**, R1079-R1090 (2011).

36. Levine J, Avrillon S, Farina D, Hug F, Pons JL. Two motor neuron synergies, invariant across ankle joint angles, activate the triceps surae during plantarflexion. *Journal of Physiology-London* **601**, 4337-4354 (2023).

37. Arakawa T, Campisi E, Tran J, Agur AMR. Dissection, digitization, and three-dimensional modelling: a high-fidelity anatomical visualization and imaging technology. *Anat Sci Int* **98**, 337-342 (2023).

38. De Oliveira DS, Carbonaro M, Raiteri BJ, Botter A, Ponfick M, Del Vecchio A. The discharge characteristics of motor units innervating functionally paralyzed muscles. *J Neurophysiol* **133**, 343-357 (2025).

39. Grison A*, et al.* Intramuscular microelectrode arrays enable highly-accurate neural decoding of hand movements. *arXiv preprint arXiv:241011016*, (2024).

40. Charles J, Kissane R, Hoehfurtner T, Bates KT. From fibre to function: are we accurately representing muscle architecture and performance? *Biol Rev* **97**, 1640-1676 (2022).

41. Ma S*, et al.* Conditional generative models for simulation of EMG during naturalistic movements. *IEEE Trans Neural Networks Learn Syst*, (2024).

42. Xia M, Chen C, Xu Y, Li Y, Sheng X, Ding H. Extracting individual muscle drive and activity from high-density surface electromyography signals based on the center of gravity of motor unit. *IEEE Trans Biomed Eng* **70**, 2852-2862 (2023).

43. Mastropietro A, Scifo P, Rizzo G. Quantitative comparison of spherical deconvolution approaches to resolve complex fiber configurations in diffusion MRI: ISRA-based vs L2L0 sparse methods. *IEEE Trans Biomed Eng* **64**, 2847-2857 (2017).

44. Manjon JV, Coupe P, Concha L, Buades A, Collins DL, Robles M. Diffusion weighted image denoising using overcomplete local PCA. *PLoS ONE* **8**, (2013).

45. Li Y*, et al.* Tracking forearm muscle fibers from diffusion MRI during dynamic contractions. In: *The 31st Annual Meeting of ISMRM*) (2022).

46. Izatt MT, Lees D, Mills S, Grant CA, Little JP. Determining a reliably visible and inexpensive surface fiducial marker for use in MRI: a research study in a busy Australian Radiology Department. *Bmj Open* **9**, (2019).

47. Leemans A, Jones DK. The B-Matrix must be rotated when correcting for subject motion in DTI data. *Magn Reson Med* **61**, 1336-1349 (2009).

48. Schneider CA, Rasband WS, Eliceiri KW. NIH Image to ImageJ: 25 years of image analysis. *Nat Meth* **9**, 671-675 (2012).

49. Yin Z, Chen C, Kang Y, Ding H, Zhu X, Meng J. A blind source separation algorithm for decoding the mechanical spatiotemporal responses of motor units. *Science China-Technological Sciences* **68**, (2025).

50. Zheng Y, Hu X. Concurrent estimation of finger flexion and extension forces using motoneuron discharge information. *IEEE Trans Biomed Eng* **68**, 1638-1645 (2021).

51. Farnebäck G. Two-frame motion estimation based on polynomial expansion. In: *Image Analysis, Proceedings* (eds Bigun J, Gustavsson T) (2003).

52. Konstantin A, Yu T, Le Carpentier E, Aoustin Y, Farina D. Simulation of motor unit action potential recordings from intramuscular multichannel scanning electrodes. *IEEE Trans Biomed Eng* **67**, 2005-2014 (2020).

53. Ferrante E, Paragios N. Slice-to-volume medical image registration: A survey. *Med Image Anal* **39**, 101-123 (2017).

54. Bolsterlee B, D'Souza A, Gandevia SC, Herbert RD. How does passive lengthening change the architecture of the human medial gastrocnemius muscle? *J Appl Physiol* **122**, 727-738 (2017).

55. Yeh F-C, Verstynen TD, Wang Y, Fernandez-Miranda JC, Tseng W-YI. Deterministic diffusion fiber tracking improved by quantitative anisotropy. *PLoS ONE* **8**, (2013).

56. Lee D, Li Z, Sohail QZ, Jackson K, Fiume E, Agur A. A three-dimensional approach to pennation angle estimation for human skeletal muscle. *Comput Methods Biomech Biomed Eng* **18**, 1474-1484 (2015).

57. Dietrich O, Raya JG, Reeder SB, Reiser MF, Schoenberg SO. Measurement of signal-to-noise ratios in MR images: Influence of multichannel coils, parallel imaging, and reconstruction filters. *J Magn Reson Imaging* **26**, 375-385 (2007).

58. Froeling M, Nederveen AJ, Nicolay K, Strijkers GJ. DTI of human skeletal muscle: the effects of diffusion encoding parameters, signal-to-noise ratio and T-2 on tensor indices and fiber tracts. *NMR Biomed* **26**, 1339-1352 (2013).

Figures

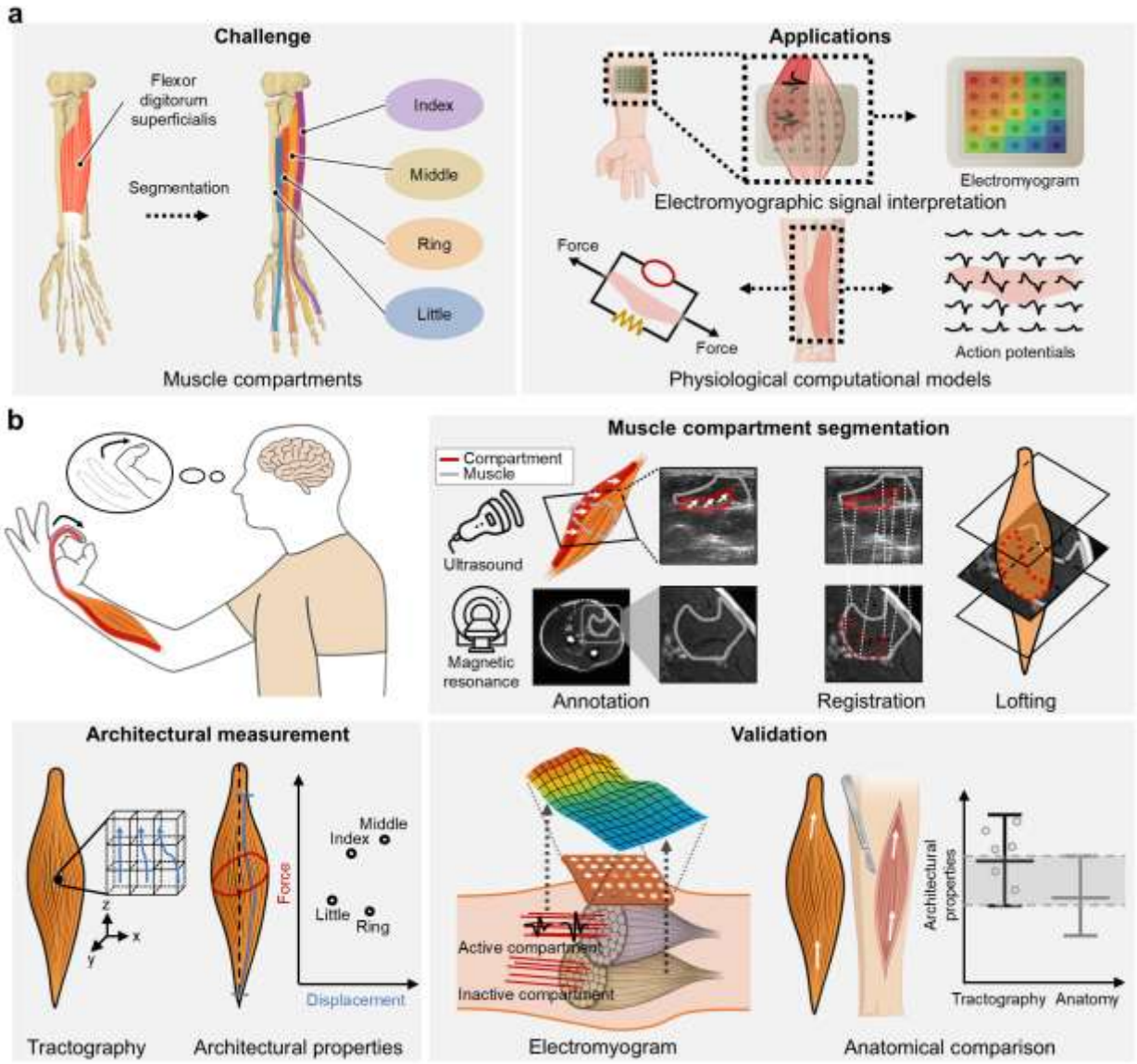


Fig. 1 | Volumetric segmentation of finger-specific muscle compartments and its validation and applications. a, Challenge and application scenarios. Localizing the muscle compartments of the finger flexor, referred to as compartment segmentation, remains challenging. Precise compartment segmentation can be applied in the following scenarios. (1) **Electromyogram (EMG) interpretation:** mapping compartment distribution to EMG activation patterns to assist in source identification. (2) **Physiological computational models:** incorporating musculoskeletal elements for biomechanical estimation, as well as EMG simulation by combining fiber tracking with action potential propagation. **b, Method design and validation.** During individual-finger movement experiments, ultrasound was used to identify the distinct motion trajectories of each compartment, thereby delineating compartment boundaries (red). The anatomical muscle boundary (grey) was defined respectively by ultrasound and magnetic resonance imaging (MRI). Multi-plane images were registered and fused from ultrasound to MRI to reconstruct the 3D volume of muscle compartments. Tractography using diffusion tensor imaging was employed to quantify architectural parameters for functional inference, and the displacement and force capacities of different finger compartments were ranked. Segmentation accuracy and functional inference were respectively validated against EMG and anatomical references.

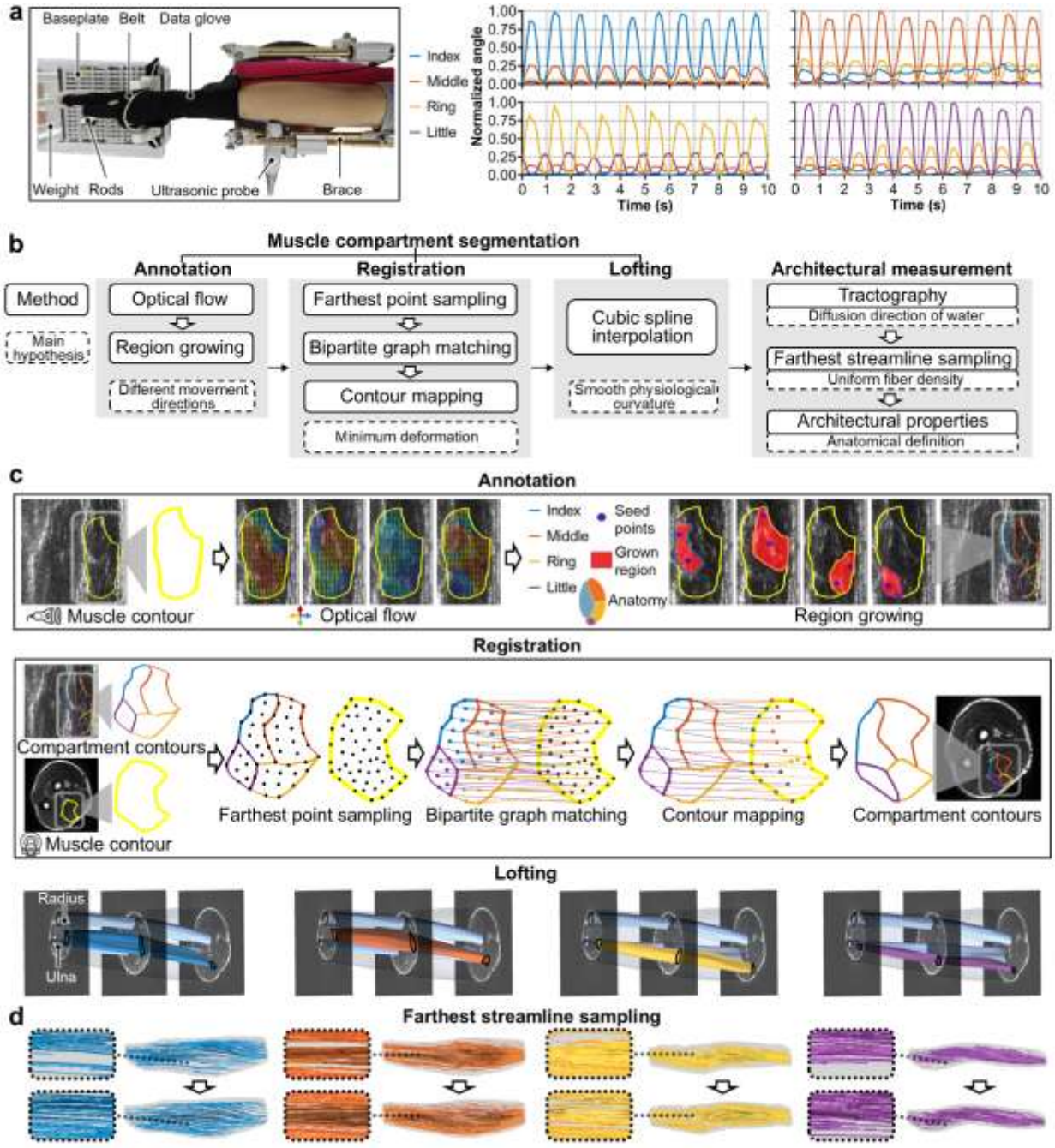


Fig. 2 | Workflow of 3D reconstruction of muscle compartments. a, Experimental setup and task. Ultrasound imaging was used to acquire data from the flexor digitorum superficialis in the forearm, while a data glove recorded the movements of four fingers (excluding the thumb). Participants performed individual-finger movements at 1 Hz, guided by a metronome, with the remaining fingers restrained by the customized platform. Normalized angles of proximal interphalangeal joint illustrate the digitization of finger motion. **b, Segmentation and registration pipeline: Annotation → Registration → Lofting → Architectural measurement. c, Details of annotation, registration and lofting.** Annotation was performed on ultrasound images. The schematic illustrates finger and muscle boundaries, seed points, grown regions, and anatomical references. In the registration step, farthest point sampling and bipartite graph matching were employed to establish spatial correspondence between the two images. Compartment contours derived from ultrasound were then mapped onto magnetic resonance images through contour mapping, thereby ensuring a consistent cross-modal framework for lofting. The unified magnetic resonance coordinate system served as the basis for 3D reconstruction. Lofting generated smooth and continuous 3D compartment volumes by spline-interpolating cross-sectional contours. **d, Representative fiber sampling.** Farthest streamline sampling was applied to obtain a uniformly distributed representative fiber set, suitable for subsequent calculation of architectural properties.

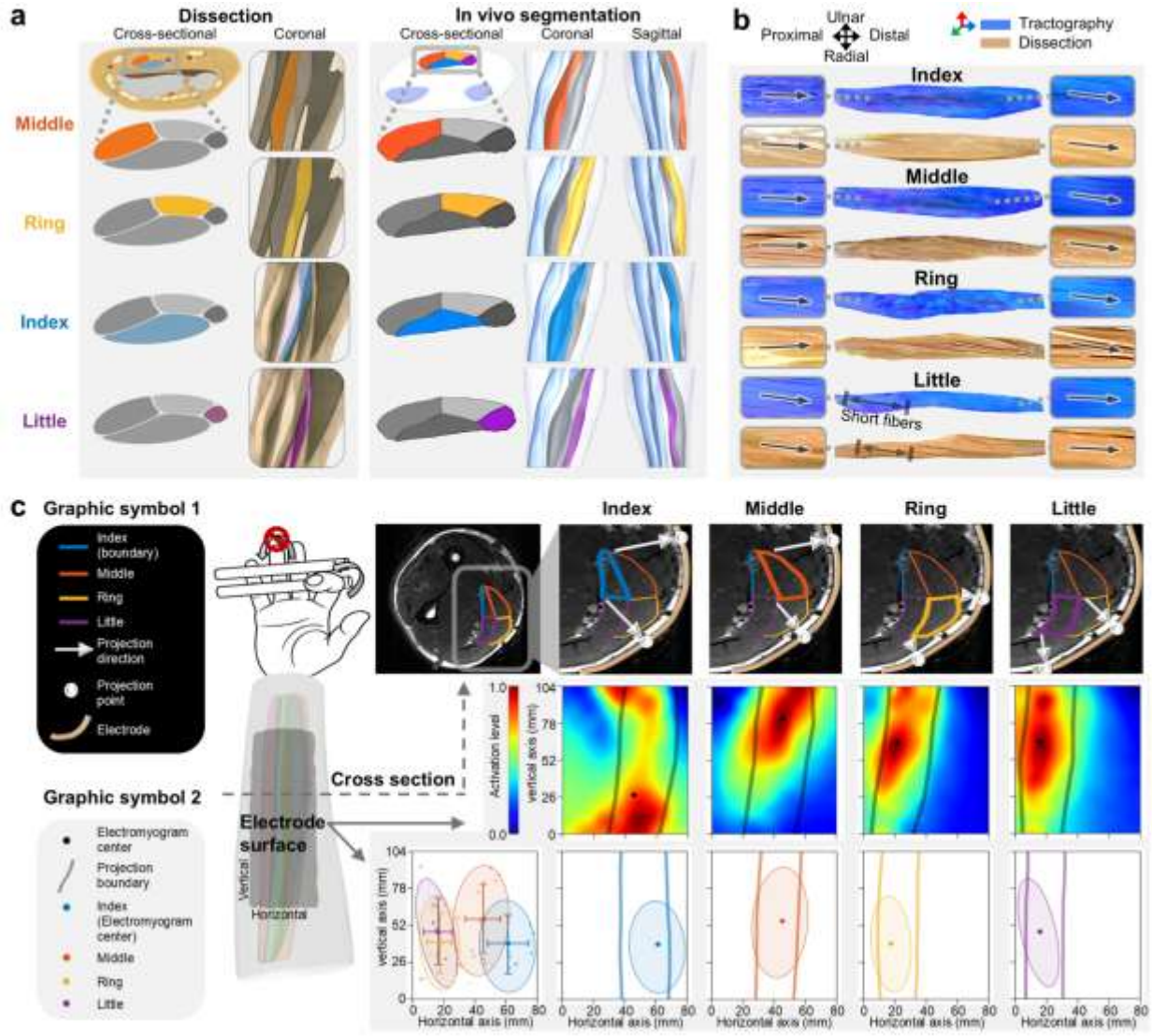


Fig. 3 | Anatomical and functional validation for compartment segmentation. a, Relative positions. The relative positions of the four muscle compartments were compared with those of anatomy (with permission) along the radial–ulnar and superficial–deep axes, validating the topological correctness of the segmentation. **b, Muscle fiber orientations.** Fiber orientations obtained from tractography and cadaveric dissection (with permission) were compared to assess the accuracy of fiber tracking within each compartment. **c, Concordance between compartment location and electromyogram (EMG) activation patterns.** High-density surface EMG maps acquired during individual-finger tasks were superimposed with the spatial boundaries of compartments. The results showed that the EMG activity centers consistently fell within the corresponding compartments.

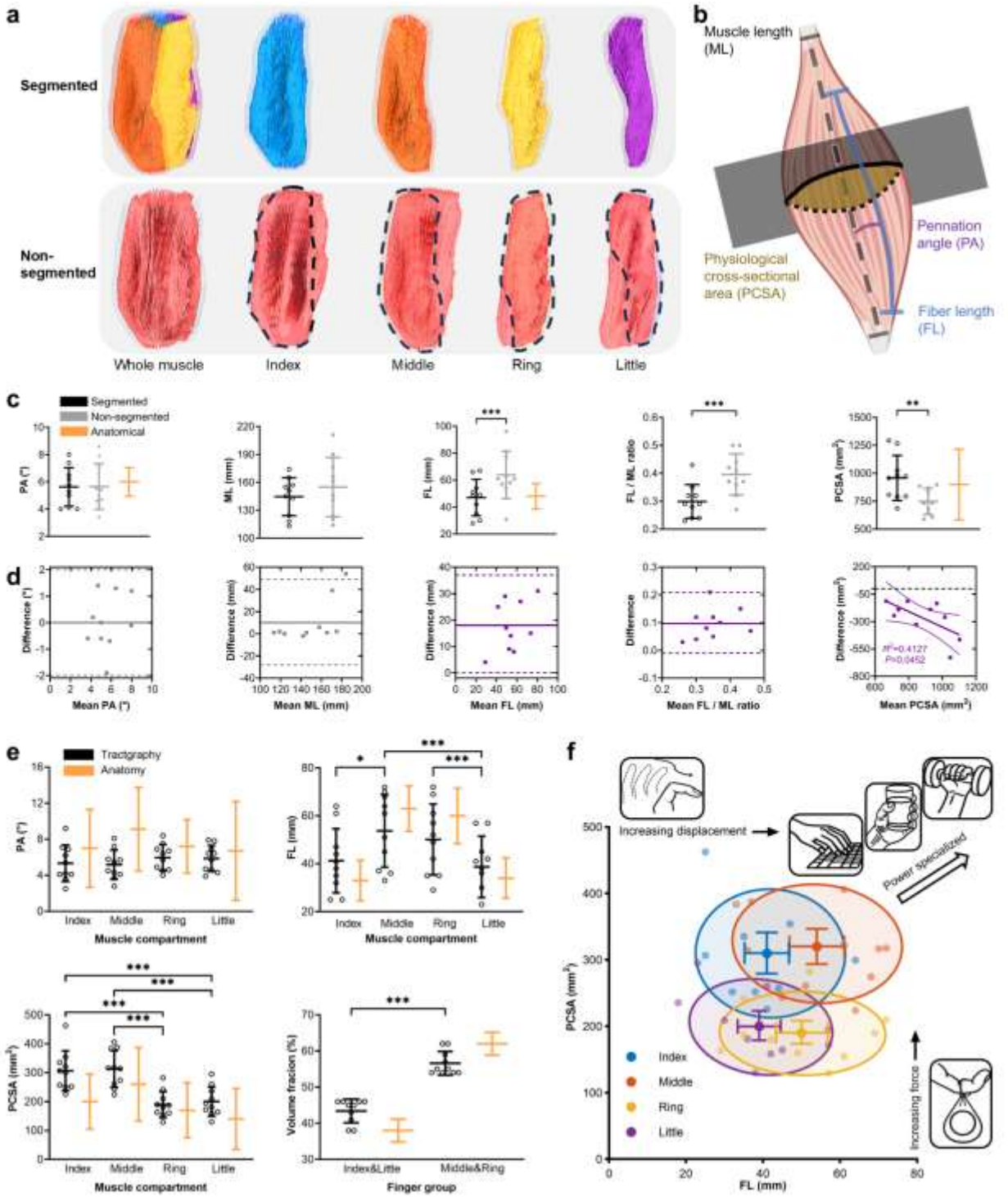


Fig. 4 | Compartment constraints improve fiber tractography and architectural measurement, and architectural properties reveal finger-specific functional roles. a, Segmented versus non-segmented tractography. Muscle fibers were reconstructed within the compartment masks in segmented tractography, whereas fibers were reconstructed within the whole-muscle mask in non-segmented tractography. Finger-specific fibers were extracted by selecting all streamlines passing through the compartment masks for the non-segmented results. Dashed lines denote compartment boundaries obtained by segmentation. The non-segmented tractography yielded fibers that inappropriately crossed compartment borders, highlighting the necessity of compartment constraints for reconstructing compartment-specific fibers. **b, Anatomical definition of architectural parameters.** A schematic illustrates measurement methods for four architectural parameters: fiber length (FL), pennation angle (PA), muscle length (ML), and physiological cross-sectional area (PCSA). **c, Comparison of flexor digitorum superficialis (FDS) architecture: segmented tractography, non-segmented**

tractography, and anatomical reference. Five parameters (PA, ML, FL, FL/ML ratio, and PCSA) were compared across the three methods. Segmented tractography yielded measurements more consistent with anatomy, whereas non-segmented tractography showed larger deviations. **d, Bland–Altman analysis of FDS architectural parameters.** Segmented and non-segmented methods were paired for Bland–Altman analysis of the five parameters, quantifying mean bias and limits of agreement to assess methodological differences. **e, Compartment-specific architectural parameters.** Architectural parameters of the compartments derived from segmented tractography were compared with anatomical references in ten participants. **f, Functional space of muscle compartments.** Functional properties of compartments were mapped in a 2D space defined by PCSA (y-axis, force capacity) and FL (x-axis, displacement capacity). The four finger compartments were localized in this space. The product of PCSA and FL approximated power output, with increasing power specialization represented by progression along the diagonal axis. In comparison, the index and middle fingers are specialized for force and power. The middle and ring fingers have a greater ability to displace.

Supplementary Files

This is a list of supplementary files associated with this preprint. Click to download.

- SupplementaryMovie3.mp4
- SupplementaryMovie4.mp4
- SupplementaryMovie2.mp4
- SupplementaryMovie5.mp4
- SupplementaryMovie1.mp4
- SupplementaryData1.zip
- SupplementaryMaterials.docx